Journal of Advanced Ceramics
2019, **8**(4): 564–575
https://doi.org/10.1007/s40145-019-0340-6

ISSN 2226-4108
CN 10-1154/TQ

Research Article

Bending fracture behavior of freestanding $(Gd_{0.9}Yb_{0.1})_2Zr_2O_7$ coatings by using digital image correlation and FEM simulation with 3D geometrical reconstruction

Weiguo MAO[a], Yujie WANG[a], Jun SHI[a], Huiyu HUANG[a], Yuncheng WANG[b], Liang LV[b], Haoyong YANG[a], Chen ZOU[a], Cuiying DAI[a,*], Xiaolei ZHU[c,*], Daining FANG[d]

[a]*School of Materials Science and Engineering*, *Xiangtan University*, *Xiangtan 411105*, *China*
[b]*Department of Science and Technology Engineering*, *AECC South Industry Co*., *Ltd*., *Xiangtan 412002*, *China*
[c]*School of Mechanical and Power Engineering*, *Nanjing Tech University*, *Nanjing 210009*, *China*
[d]*Institute of Advanced Structure Technology*, *Beijing Institute of Technology*, *Beijing 100081*, *China*

Received: January 24, 2019; Revised: March 26, 2019; Accepted: May 10, 2019

Abstract: It is important to investigate the mechanical performances of $(Gd_{0.9}Yb_{0.1})_2Zr_2O_7$ (GYbZ) materials deposited on irregular substrates for improving new thermal barrier coatings. Three-point bending fracture characteristics of freestanding GYbZ coating prepared by supersonic plasma sprayed (SPS) technique were investigated with the help of digital image correlation technique. The cracking time, crack propagation path, and mechanical properties of GYbZ coating were obtained. Meanwhile, the X-ray computed tomography technique was introduced to scan the microstructure of freestanding GYbZ coatings, which are used to establish three-dimensional (3D) finite element model by using the Avizo software. The brittle cracking criterion was applied to describe the bending fracture process of GYbZ coatings. The critical cracking strain was estimated as 0.36%±0.03% by repeatedly comparing the difference between the experimental and simulated curves. The results would be extended to predict the dangerous region and failure mechanisms of GYbZ coatings deposited on irregular substrate during finite element simulations.

Keywords: thermal barrier coating; X-ray computed tomography; bending fracture; geometrical reconstruction; cracking strain

1 Introduction

Thermal barrier coatings (TBCs) with lower thermal conductivities and higher thermal insulation capabilities have been widely applied in gas-turbine engines and jet engines. Thermal barrier coatings consist of four layers, i.e., ceramic top-coat (TC), bond-coat (BC), thermally grown oxide (TGO), as well as superalloy substrate [1–3]. As a classical ceramic top coat material, 6–8 wt% yttria stabilized zirconia (YSZ) had attracted the attention of numerous researchers owing to its excellent properties such as low thermal

* Corresponding authors.
E-mail: C. Dai, daicuiying@xtu.edu.cn;
X. Zhu, zhuxiaolei@ njtech.edu.cn

conductivity and high thermal expansion coefficients (TECs). However, its phase transformation and sintering result in a poor performance when the service temperature exceeds 1200 ℃ [4]. Therefore, in recent years, many researchers developed rare-earth doped zirconia and zirconate TBCs, such as ScGdSZ [5], $La_2Zr_2O_7$ [6,7], and $Gd_2Zr_2O_7$ [8–13]. Zhang *et al*. [14] systematically investigated the thermophysical properties of Yb_2O_3 doped $Gd_2Zr_2O_7$ and obtained many interesting results. They found that $(Gd_{1-x}Yb_x)_2Zr_2O_7$ exhibited lower thermal conductivities and higher thermal expansion coefficients (TECs) than $Gd_2Zr_2O_7$. The TECs increase with the increasing of Yb_2O_3 contents. $(Gd_{0.9}Yb_{0.1})_2Zr_2O_7$ (GYbZ) ceramic exhibited the lowest thermal conductivity among all the ceramics studied, within the range of 0.8–1.1 W/(m·K) (20–1600 ℃). The results of thermal cycling tests show that the GYbZ/YSZ double-ceramic-layer coatings have a more extended lifetime than the single YSZ coatings [14,15]. It may be attributed to excellent thermal insulation properties and high coefficient of thermal expansion of GYbZ coating.

Generally, most TBCs systems in practice have complex and irregular geometrical structures, it is difficult to estimate their reliability and durability using experimental methods and analytical solutions. It is necessary to develop finite element method (FEM) to predict the failure mechanisms and danger region of TBCs deposited on irregular geometric metal components [16]. Over the past decades, many scholars used FEM to study the multiple fragmentation and failure analysis of TBCs. An attempt was made to overcome the actual complex surface topography by generating finite element geometrical model of the TBCs based on actual 2D microstructure images, and the growth of micro-cracks was clearly observed during the simulation [17,18]. The interface fracture toughness and actual interface morphology of the TBCs system were investigated and observed, then micro-computed tomography was used to observe the evolution of microstructure and reveal the failure mechanisms [19–23]. Li *et al*. [24] analyzed the residual stress distributions based on the real three-dimensional (3D) images using computed tomography, and discussed the accurate strain gradient distribution measurements as a function of depth in TBCs systems. Fan *et al*. [25,26] studied the effect of TGO on the multiple surface cracking behaviors in an air plasma sprayed (APS) TBCs by using extended finite element method (XFEM). Zhu *et al*. [27,28] established a finite element model to evaluate the stress distributions and simulated spallation of TBCs with two-dimensional (2D) real TGO morphology under thermal stress. Jiang *et al*. [29] analyzed the residual stress and top coat cracking behavior in TBCs under cyclic thermal loading by FEM with the cohesive zone model. Zhu *et al*. [30] determined the interfacial residual stress in TBCs by using FEM analysis and digital image correlation method. In addition, most of work studied the mechanical properties of composite materials by using X-ray tomography and finite element mesh models [31–34]. However, true TBCs structures have a lot of pores, micro-cracks, and different crystallization orientation. As we know, little FEM work reported the effect of real defects on fracture failure of GYbZ TBCs based on 3D geometrical reconstruction.

The aim of this paper is to analyze three-point bending failure process of GYbZ coating using X-ray micro-computed tomography and FEM techniques, and estimate the key failure parameters of FEM corresponding to the fracture GYbZ coating. Three-point bending fracture tests of freestanding GYbZ coating prepared by supersonic plasma sprayed (SPS) were studied with the aid of digital image correlation (DIC). The cracking time, crack propagation path, and mechanical properties of GYbZ coating were obtained. Meanwhile, the real structure of GYbZ coating specimen was firstly scanned using X-ray micro-computed tomography. All images were digitally processed with Avizo tool. 3D geometrical reconstruction model was obtained and imported into the commercial ABAQUS. The brittle cracking criterion in FEM was applied to judge the cracking nucleation, propagation, and fracture of GYbZ coating during bending tests. The necessary parameters of brittle cracking criterion in FEM were evaluated by repeatedly comparing the difference between experimental and simulated curves. The results will provide useful guidance for improving finite element simulation accuracy of the GYbZ TBCs failure mechanism with irregular geometric configurations.

2 Materials and methods

2.1 Materials and sample preparation

GYbZ ceramics were produced by making use of solid-state reaction method, using Gd_2O_3, Yb_2O_3, and ZrO_2 (≥ 99.99%) powders as original materials [14,15]. GYbZ powder was sprayed onto a medium carbon steel plate by SPS technique with a Metco-Triplex I plasma torch (Sulzer Metco, Winterthur, Switzerland).

The detailed preparation parameters are shown in Table 1. In order to avoid the effects of the underlying substrate, the coated steel substrate was cut into small strips of the specified size using commercial cutter (IsoMet 4000). The steel substrate was etched with dilute hydrochloric acid solution and freestanding GYbZ coating specimens were obtained. Then, three samples were cut into 30 mm×6 mm×3 mm for bending tests. In order to remove the influence of dilute hydrochloric acid solution soaking, freestanding GYbZ samples were cleaned with deionized water, acetone, and ethanol, in sequence, then dried.

2. 2 Three-point bending tests

Three-point bending tests of freestanidng GYbZ coating were performed by utilizing universal testing machine (WDT115) at loading rate of 0.05 mm/min. Here the span was 20 mm. The schematic diagram and experimental apparatuses of three-point bending tests are shown in Fig. 1. Meanwhile, the micro-scale speckle patterns were fabricated and optimized by spinning an epoxy resin and powder for DIC measurements [35]. According to the micrographs of the patterned surface, the evolution of strain and cracking of each sample was *in situ* monitored and recorded by utilizing a charge-coupled device camera (GOM Co., Germany) with resolution of 1624 pixel × 1236 pixel, performed a sample rate of one image per second. The detailed strain fields and fracture information were evaluated through the relevant DIC software (ARAMIS) post-processing.

Table 1 Preparation parameters of GYbZ coating by SPS

Parameter	Supersonic plasma sprayed for TC
Gun	HEPJet
Power (kW)	50–80
Max. current (A)	600
Max. voltage (V)	220
Distance (mm)	80–110
Ar/H_2 (SLPM)	60–90
Feed rate (g/min)	30–60
Particle velocity (m/s)	400–450
Oxygen (SCPH)	—
Carrier gas (NLPM)	—

All experimental data including critical fracture load, strain fields, fracture time, and cracking behavior, can be obtained from the aforementioned tests, which are used to analyze the mechanical properties of GYbZ samples. Bending strength (σ_b) and Young's modulus (E) can be obtained by the following equations [36].

$$\sigma_b = \frac{3FL}{2Bw^2} \tag{1}$$

$$E = \frac{L^3 m}{4Bw^3} \tag{2}$$

where F denotes the peaking load, L is the size of the span, B and w are the width and thickness of the specimen, respectively. m is the slope of the tangent to the initial linear part of the load-deflection curve. σ_b and E as critical parameters would be imported into the subsequence FEM simulation.

3 3D geometrical reconstruction

3. 1 X-ray computed micro-tomography scanning

X-ray computed micro-tomography (X-ray μCT, No. 600 kV/225 kV dual source industrial DR/CT) is one

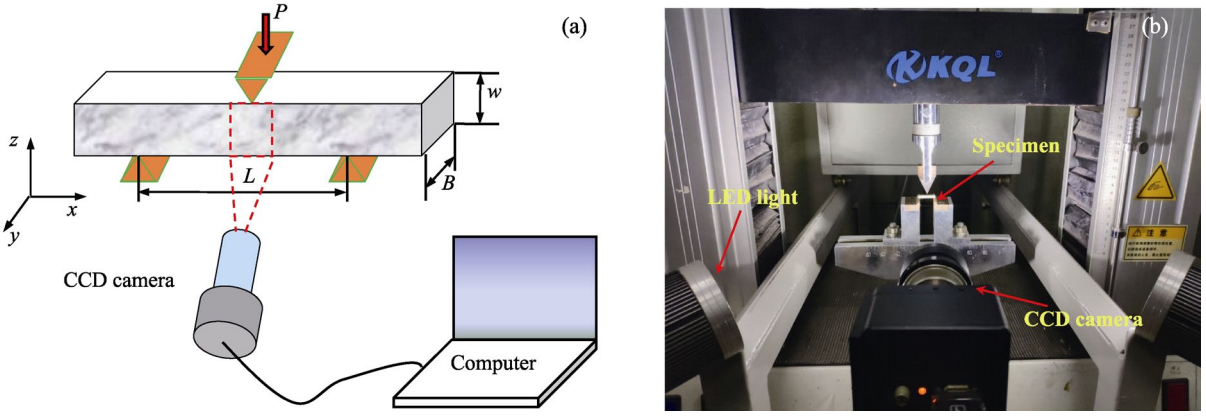

Fig. 1 (a) Schematic of three-point bending test with the aid of DIC and (b) the experimental system.

of the most promising high-resolution non-destructive imaging techniques, and it has been extensively applied to detect the internal defects in materials by utilizing the high fluxes from synchrotron sources [37–40]. The schematic diagram of the micro-focus X-ray CT is illustrated in Fig. 2. A bundle of X-ray sources penetrates through the object along different paths during the rotating of the sample, then is projected on the detector to obtain a series of 2D projection photographs by computer processing. It is important to choose the right sample size or scan parameters to obtain high-quality projection images due to the strong X-ray attenuation characteristics of GYbZ coating. Here, the size of the scanned sample was designed as 35 mm×2.5 mm×1.5 mm. The accelerating voltage and tube current were 160 kV and 500 μA, respectively. For each projected photograph, the scanning time was set as 1000 ms. The minimum pixel size was about 11 μm by using 18 geometrical magnification. The total 500 slice images were obtained through the reconstruction of X-ray data and stored in tiff file format.

3. 2 CT image processing

Compared to traditional surface characterizations of TBCs, the volumetric data from CT scanning has been widely used to quantitatively analyze the internal microstructural features of the GYbZ coating, such as micro-cracks and large voids (> 50 μm), as well as fracture surface [41,42]. However, the limited resolution prevented the analysis of clear images and even affected the understanding of failure modes of GYbZ coatings. Therefore, in order to enhance the quality in 2D images, all tomographic photographs were digitally processed with a commercial Avizo software (FEI, version 9). The detailed processing workflow is listed in Fig. 3. Thresholding and segmentation techniques were implemented to distinguish different items (micro-cracks and material). The original picture obtained from the CT facility is shown in Fig. 4(a). These images show that there are a large number of intrinsic micro-cracks on the GYbZ samples during the preparation process, which severely shorten the service lifetime of the GYbZ coating. The GYbZ material is presented by light grey or white (high intensity voxels) and the micro-cracks are described by black color (low intensity voxels). To extract or clearly distinguish microscopic defects (mainly micro-cracks) in the original image as much as possible, each digital image was processed with the following procedures. All original pictures were firstly processed into grayscale images with 256 gray levels. The grayscale images were enhanced to eliminate the related noise for clear boundaries and complete contours. They were transformed into binary images by attaching the interactive thresholding module of the Avizo software, where the value of the threshold is set as 29 during the binarization processing analysis. It is noted that the thresholds for each image were adjusted to distinguish the micro-cracks and large voids in the GYbZ coating. However, when the acquisition data is too coarse or noisy, thresholding cannot distinguish boundary or contour owing to the gray levels of the considered objects are not uniform enough across the volume, or some objects' boundaries cannot be distinguished because

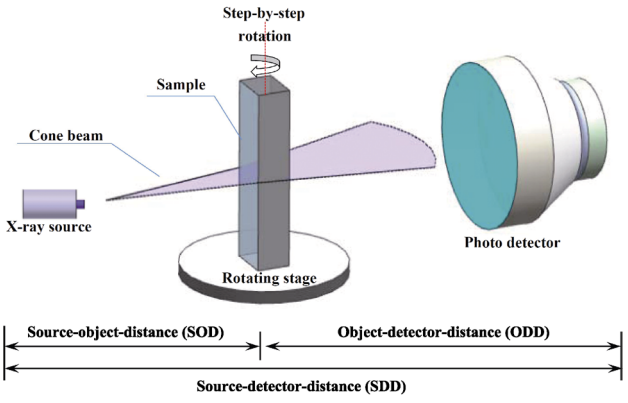

Fig. 2 Schematic of the X-ray CT acquisition process, where the SOD and ODD are 105 and 189 mm, respectively.

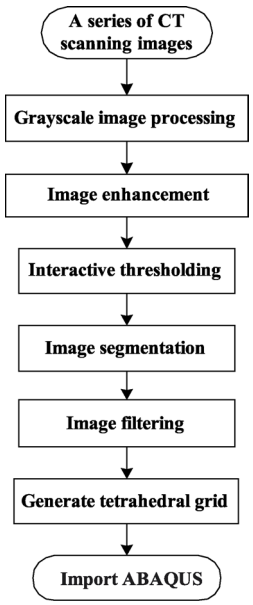

Fig. 3 Processing workflow of the X-ray μCT images by using the Avizo software.

the resolution is too low. Therefore, it is found that the separation by connecting a separate-objects module to the thresholded data plays an important role in compensating the GYbZ coating images with too low resolution, noise, and intensity. Meanwhile, the image separation was performed using watershed algorithm. In some cases, it may be necessary to proceed to semi-automatic or manual segmentation, where semi-automatic segmentation was used in this article. Furthermore, the median filter process was used to preserve edges while removing noise. The interesting area and useful information are found after the above steps, and the cracking information can be extracted through the image processing method, as shown in Fig. 4(b).

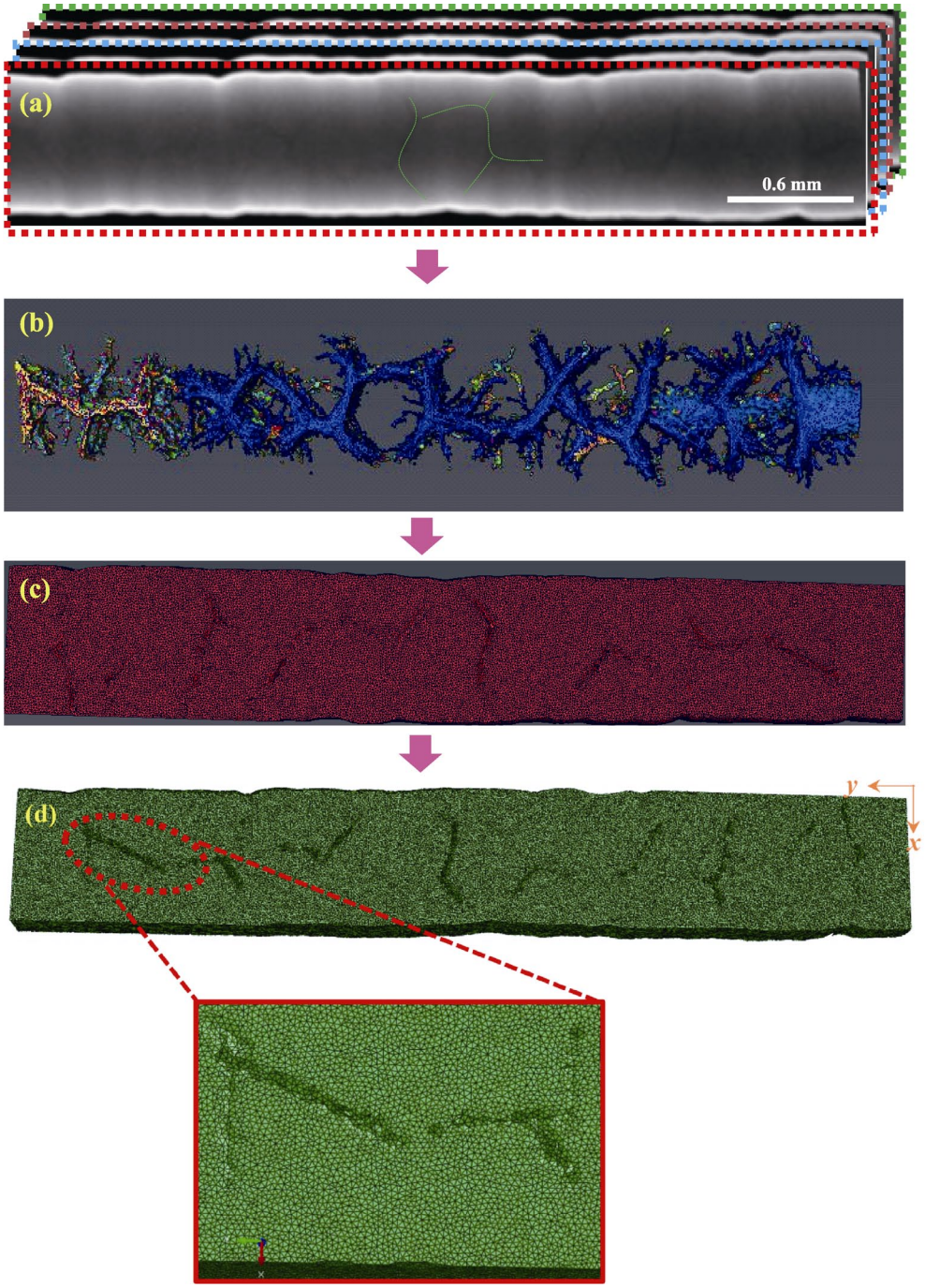

Fig. 4 Finite element modeling process of GYbZ coating with a commercial Avizo software: (a) The original images obtained from the X-ray μCT, (b) the internal true structure of GYbZ coating after the image processing, (c) superficial mesh processing of GYbZ coating sample, and (d) FEM meshes of GYbZ coating sample, where a representative region with dashed elliptical is enlarged, as shown in inset.

3. 3 3D reconstruction

The tomographic images were permitted for producing a 3D view and reconstructed using Avizo software. The generation process includes the following steps, extracting the surface from the segmentation result by connecting a generate surface module to the segmentation data. Owing to the number of triangles created by the generate surface module is far too large for subsequent operations, it is indispensable to use surface simplification module to reduce the number of triangles. Some indistinguishable cracks and holes were inevitably ignored during this simplification process. In contrast, the reconstructed model for CT analysis was simplified, and the combined FEM and DIC experiments will provide more quantitative data in subsequent analysis. It is noted that the orientation of a few triangles may be inconsistent after surface simplification, resulting in partial overlap of the GYbZ material defined by the triangles. Therefore, it is necessary to use manual operations to repair. At last, 3D geometrical superficial meshes of GYbZ coating specimen with true microscopic defect (mainly cracks and micro-voids) distribution, which was determined to be a reconstruction artifact, can be obtained, as shown in Fig. 4(c).

However, the superficial mesh (triangular elements) cannot be used for finite element simulations. Therefore, it is essential to use the self-adaptive delaunay algorithm to generate a volumetric tetrahedral grid from the triangular surface for numerical simulations. And the specific examinations are useful for preparing a tetrahedral grid generation. During this process, we need to check the aspect ratio of the triangle mesh and the dihedral angle among the triangle meshes by using surface/tests module. It is found that the largest aspect ratio should be below 20 (better below 10). The smallest dihedral angle should be larger than 5° (better larger than 10°) [43]. On the contrary, it can result in intersecting triangles and affect mesh quality. Finally, the volumetric tetrahedral grid was generated by attaching the generate tetra grid module, as shown in Fig. 4(d). Similarly, the tetrahedral quality tests are indispensable. The largest tetrahedral aspect ratio should be below 50 (better below 25) to eliminate the non-convergence in numerical simulations as much as possible. After the aforementioned operations, it means that the volume enclosed by the surface was filled with tetrahedra. The examination of the reconstructed volume indicates that the microstructure characteristics can be easily distinguished based on the transparency of the X-ray illumination [42]. The INP file was exported from the Avizo software and imported into the ABAQUS program for numerical simulation.

4 Results and discussion

4. 1 SEM observations of freestanding GYbZ coating

Figure 5 displays SEM images on the polished surface of three as-sprayed freestanding GYbZ coatings. Owing to the extremely high cooling rate in the particles during the plasma sprayed process, sufficient adhesion cannot be established among the deposited particles. For as-prepared samples, a large number of inherent cracks and pores exist. The porosity of the GYbZ coating was analyzed by using commercial Image J software. Three sample porosities are about 10.4%, 9.6%, and 8.4%, respectively. The average porosity of as-sprayed freestanding GYbZ coating is about 9.5%. EDS analysis shows that the GYbZ coating mainly contains 30% O, 41% Zr, 24% Gd, and about 1% Yb, which indicates it has relatively few impurities during the preparation process.

4. 2 Bending fracture tests of freestanding GYbZ coating

Figure 6 displays the representative axial strain mappings (ε_{xx}), of three GYbZ coating specimens during three-point bending tests. In Fig. 6(a), it can be seen that the time corresponding to cracking nucleation and rupture is 90 and 187 s, respectively, and the critical bending load is 21.5 N. Similarly, it is shown in Figs. 6(b) and 6(c) that the cracking nucleation time is 93 and 94 s, respectively. It means that the quality consistency of GYbZ coating specimens is good. As bending loads increase, *in situ* DIC analysis reveals that the crack first forms close to the maximum bending moment location and propagates along the thickness direction. The experimental data including bending load, failure strain, and time were recorded by computer and used to evaluate σ_b and E. The critical strain corresponding to cracking formation can be estimated from DIC analysis. The average value is about 0.33%±0.04%. Therefore, the average σ_b and E of three GYbZ coating specimens can be obtained about 12 MPa and 3.86 GPa by Eqs. (1) and (2), respectively.

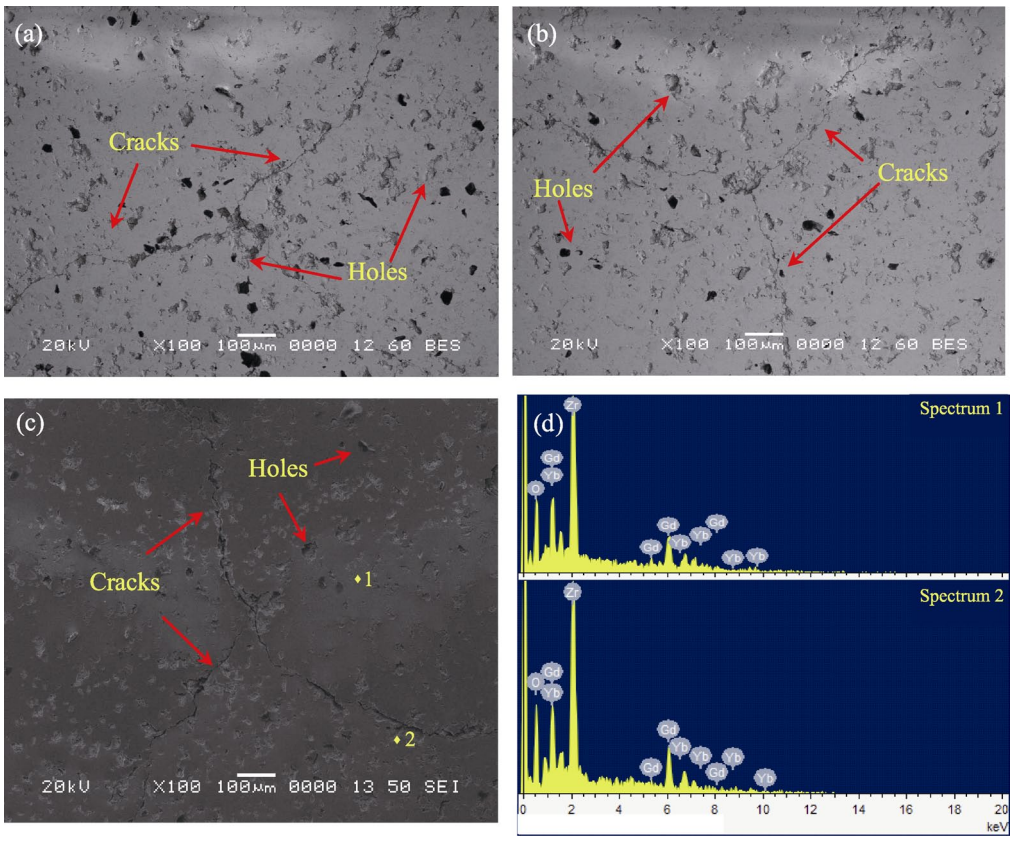

Fig. 5 SEM micrographs of the polished surface of as-sprayed freestanding GYbZ coating: (a) 1# specimen, (b) 2# specimen, and (c) 3# specimen. (d) EDS spectra of the GYbZ coating components.

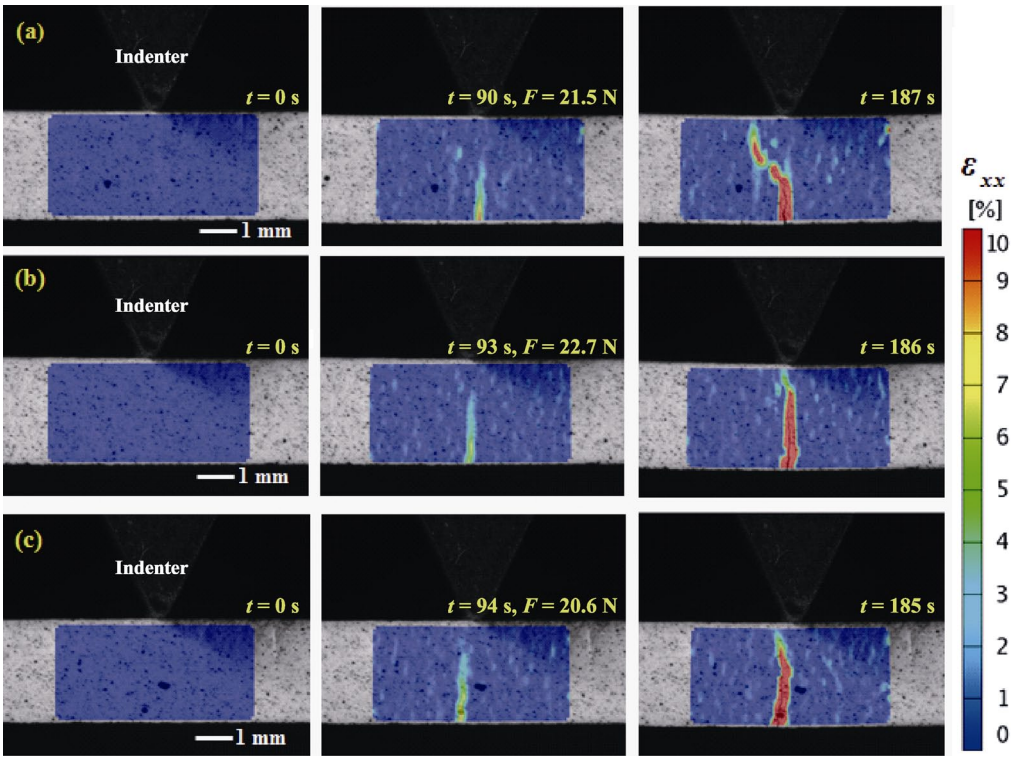

Fig. 6 Evolution of strain mapping of three GYbZ coating samples during bending tests: (a) 1# specimen, (b) 2# specimen, and (c) 3# specimen. Here *F* denotes the breaking load, corresponding to the cracking nucleation.

The stress in the GYbZ coating beneath the neutral layer is tensile state during three-point bending fracture process. Generally, this tensile stress is easier to induce the nucleation and propagation of the primary cracking, as shown in Fig. 6. The maximum stress or moment locates in the central of the sample, where the first crack forms. With the increasing of bending loads, the crack gradually grows. In addition, DIC analysis shows that the crack path is affected by the microstructure, pores and voids in the GYbZ coating prepared by SPS. DIC is a powerful tool for *in-situ* measurement of microstructure-processing-deformation-failure relationships of advanced ceramic or composite coatings under different scales [44–47].

4. 3 Cracking strain estimation of GYbZ coating in FEM

FEM analysis procedure for bending fracture of GYbZ coating is shown in Fig. 7. The damage behavior of GYbZ coating is simulated by ABAQUS/Explicit [48]. The indenter as well as the left and right support are defined as the analytical rigid bodies. The upper and lower surfaces of finite element model with real structure are assumed to be hard contacts. The friction coefficient of the contact surface is set to 0.05. Moreover, the element type is selected as C3D4 (tetrahedral unit). The total number of nodes and elements of the reconstructed FEM models is 98,531 and 513,978, respectively. Moreover, the average tetrahedral element volume can be approximately estimated to be 8.8±3.2 voxels.

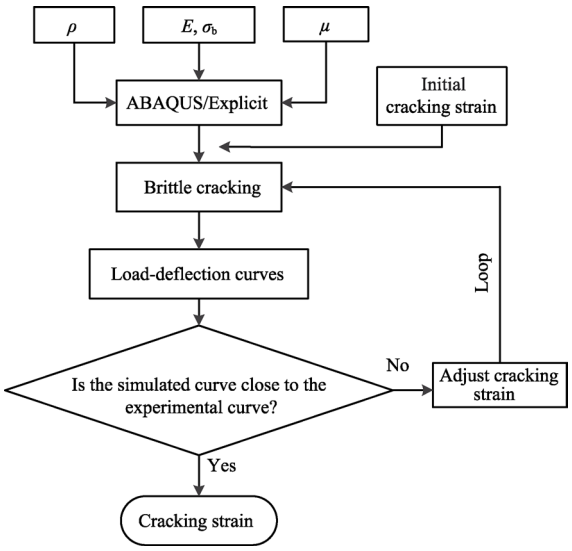

Fig. 7 Estimation procedures of the cracking strain of freestanding GYbZ coating sample by using ABAQUS.

Brittle cracking criterion is introduced to judge cracking nucleation and propagation of GYbZ coating during the FEM simulations with real structure. The necessary material parameters of FEM model including elastic modulus, Poisson's ratio, and fracture strength are obtained, where E = 3.86 GPa, μ = 0.27, σ_b = 12 MPa, and ρ = 5.89 g/cm^3 are provided by using the Archimedes drainage method [49,50]. According to the cracking strain, 0.33%±0.04%, from the DIC results, different cracking strain data are inputted to the FEM model and the corresponding bending load–displacement curve is obtained. We compare the difference between the experimental and simulated curves and estimate the optimized cracking strain.

Figure 8 presents the progressive damage process of GYbZ coating model with defects. It can be seen that the cracking configuration is similar to the experimental results presented in Fig. 6(a). To further explore the damage mechanisms of GYbZ coating, the model contains a large number of mesh defects, as shown in Fig. 4(d). The initial damage first appears between the tetrahedral element nodes and then expands along the weakest place. It is found that the mesh at the fracture surface is distorted, which may be attributed to the stress concentration. In addition, the interaction of random distributed large voids under bending loads would result in different propagation paths and fracture modes of the GYbZ coating, depending on the inter-splat boundaries orientation [51]. The FEM analysis reveals that deformation of GYbZ coating is highly sensitive to the local microstructure, as shown in Fig. 8. It can clarify the local rupture trends with the aid of DIC measurements. The cracking strain determined by DIC analysis during bending tests was 0.33%±0.04%. We attempted to set the different cracking strains within the range of 0.33%–0.48% during FEM simulations, and analyzed the difference between the experimental and simulated load–displacement curves, as shown in Fig. 9. The local cracking behaviors in the GYbZ coating were confirmed by FEM calculations. Finally, the optimized cracking strain of GYbZ coating is estimated as about 0.36%±0.03%. The corresponding critical load and fracture displacement are obtained as 20.3 N and 0.072 mm, respectively. They are in good agreement with the experimental results, 21.5 N and 0.068 mm, respectively. It can be obviously determined that the ABAQUS curve has the same behavior as the experiment, which means that the boundary conditions, material properties, and internal defects (mainly micro-cracks)

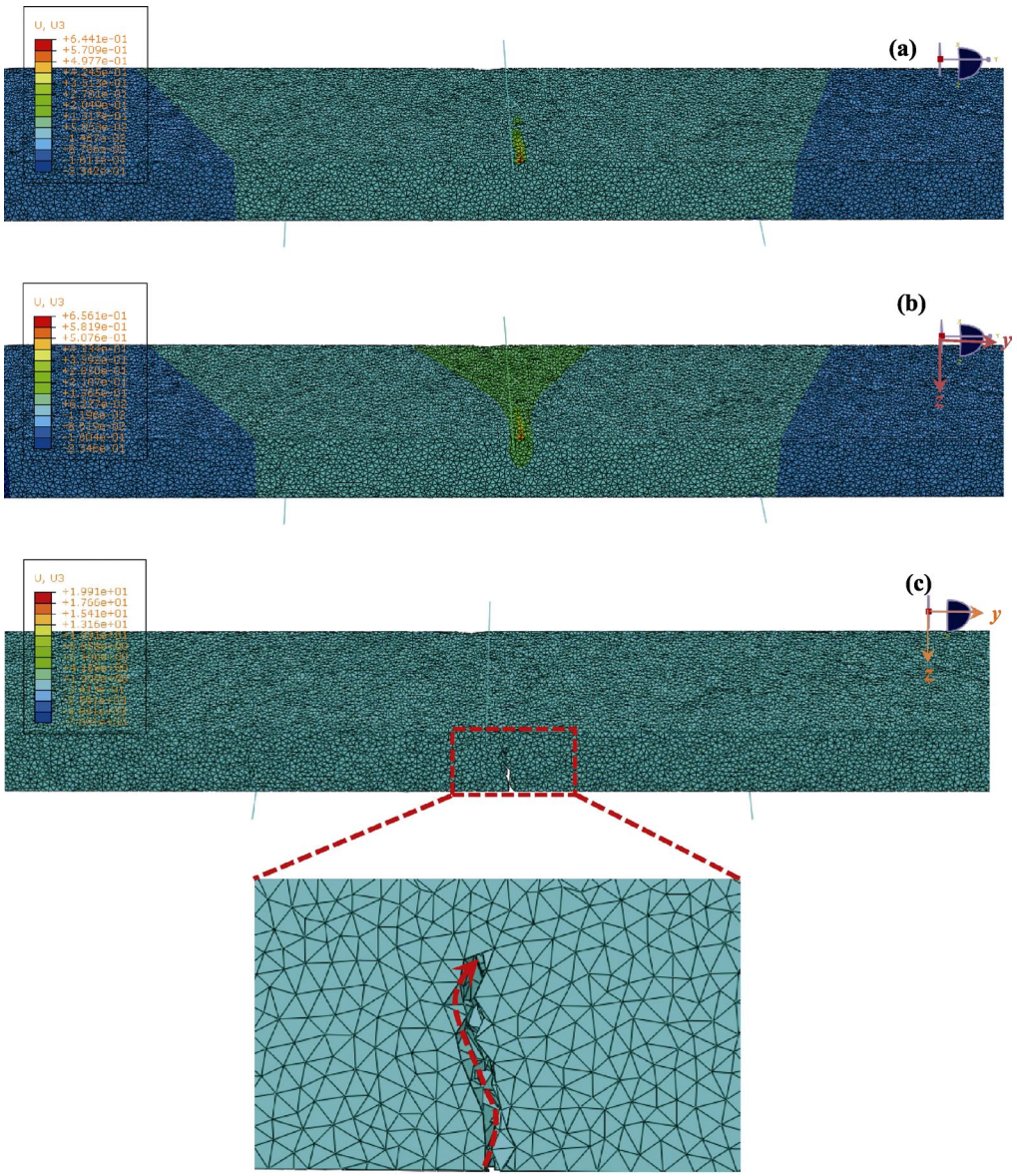

Fig. 8 Evolution of deflection of freestanding GYbZ coating during the FEM of three-point bending fracture process. The first fractured region is enlarged, as shown in inset.

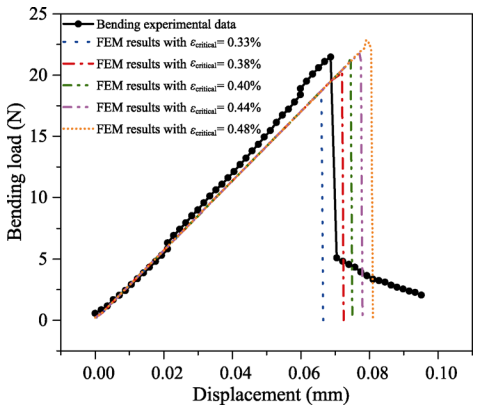

Fig. 9 Estimation of the critical cracking strain of GYbZ coating sample by FEM, comparing with the experimental data.

are successfully replicated. Therefore, the reliability and feasibility of the reconstruction model are well proved. The critical strain evaluated by FEM and experimental tests is useful for judging the delamination formation and fracture threshold for strain-based lifetime models. In addition, the 3D FEM model with true micro-crack structure of GYbZ coating will provide good guidance for predicting the service lifetime and reliability of TBCs with irregular geometry substrates.

5 Conclusions

Freestanding GYbZ coatings were prepared by SPS

technique. The bending characteristics of GYbZ coating were measured with the aid of DIC technique. The fracture strength and elastic modulus of GYbZ coating were determined as 12 MPa and 3.86 GPa, respectively. The average cracking strain of GYbZ coating was about 0.33%±0.04% by using DIC analysis. The average porosity of as-sprayed freestanding GYbZ coating was about 9.5%. Moreover, 3D finite element model with true micro-crack structure of GYbZ coating was reconstructed by using CT technique and Avizo software. The critical cracking strain of GYbZ coating evaluated in FEM simulation was about 0.36%±0.03% by progressively attempting different values, comparing with experimental load–displacement curves. It can be seen from Fig. 9 that the simulated and experimental load–displacement curves are well matched within the allowable range of the error. Thus, the reliability and feasibility of the reconstruction model are proved. The main merit of this modeling approach is that it can take into account actual defects in the model, and then can be converted to finite element meshes. Finally, the ultimate goal is to establish a FEM model of the irregular TBCs containing defects, and apply in the high temperature environment of the TBCs to accurately predict the service lifetime in the future.

Acknowledgements

This work was supported by the National Natural Science Foundation of China (Grant Nos. 11572277, 11772287, 11802260) and the Young and Middle-aged Scholar Training Program of Hunan Province Association for Science and Technology (2017TJ-Q02), the Natural Science Foundation of Hunan Province (No. 2018JJ3490), and the Research Learning and Innovative Experimental Plan for College students of Xiangtan University (No. 2017XJ033).

References

[1] Padture NP, Gell M, Jordan EH. Thermal barrier coatings for gas-turbine engine applications. *Science* 2002, **296**: 280–284.

[2] Padture NP. Advanced structural ceramics in aerospace propulsion. *Nat Mater* 2016, **15**: 804–809.

[3] Song XM, Meng FL, Kong MG, *et al.* Thickness and microstructure characterization of TGO in thermal barrier coatings by 3D reconstruction. *Mater Charact* 2016, **120**: 244–248.

[4] Mahade S, Curry N, Björklund S, *et al.* Failure analysis of $Gd_2Zr_2O_7$/YSZ multi-layered thermal barrier coatings subjected to thermal cyclic fatigue. *J Alloys Compd* 2016, **689**: 1011–1019.

[5] Sun LL, Guo HB, Peng H, *et al.* Influence of partial substitution of Sc_2O_3 with Gd_2O_3 on the phase stability and thermal conductivity of Sc_2O_3-doped ZrO_2. *Ceram Int* 2013, **39**: 3447–3451.

[6] Aruna ST, Sanjeeviraja C, Balaji N, *et al.* Properties of plasma sprayed $La_2Zr_2O_7$ coating fabricated from powder synthesized by a single-step solution combustion method. *Surf Coat Technol* 2013, **219**: 131–138.

[7] Girolamo GD, Marra F, Blasi C, *et al.* High-temperature mechanical behavior of plasma sprayed lanthanum zirconate coatings. *Ceram Int* 2014, **40**: 11433–11436.

[8] Moskal G, Swadźba L, Hetmańczyk M, *et al.* Characterization of microstructure and thermal properties of $Gd_2Zr_2O_7$-type thermal barrier coating. *J Eur Ceram Soc* 2012, **32**: 2025–2034.

[9] Drexler JM, Gledhill AD, Shinoda K, *et al.* Jet engine coatings for resisting volcanic ash damage. *Adv Mater* 2011, **23**: 2419–2424.

[10] Wang L, Guo L, Li ZM, *et al.* Protectiveness of Pt and $Gd_2Zr_2O_7$ layers on EB-PVD YSZ thermal barrier coatings against calcium-magnesium-alumina-silicate (CMAS) attack. *Ceram Int* 2015, **41**: 11662–11669.

[11] Wang L, Eldridge JI, Guo SM. Thermal radiation properties of plasma-sprayed $Gd_2Zr_2O_7$ thermal barrier coatings. *Scripta Mater* 2013, **69**: 674–677.

[12] Jackson RW, Zaleski EM, Hazel BT, *et al.* Response of molten silicate infiltrated $Gd_2Zr_2O_7$ thermal barrier coatings to temperature gradients. *Acta Mater* 2017, **132**: 538–549.

[13] Jesuraj SA, Kuppusami P, Dharini T, *et al.* Effect of substrate temperature on microstructure and nanomechanical properties of $Gd_2Zr_2O_7$ coatings prepared by EB-PVD technique. *Ceram Int* 2018, **44**: 18164–18172.

[14] Zhang HL, Guo L, Ma Y, *et al*. Thermal cycling behavior of $(Gd_{0.9}Yb_{0.1})_2Zr_2O_7$/8YSZ gradient thermal barrier coatings deposited on Hf-doped NiAl bond coat by EB-PVD. *Surf Coat Technol* 2014, **258**: 950–955.

[15] Guo L, Guo HB, Peng H, Gong SK, *et al.* Thermophysical properties of Yb_2O_3 doped $Gd_2Zr_2O_7$ and thermal cycling durability of $(Gd_{0.9}Yb_{0.1})_2Zr_2O_7$/YSZ thermal barrier coatings. *J Eur Ceram Soc* 2014, **34**: 1255–1263.

[16] Wang L, Li DC, Yang JS, *et al.* Modeling of thermal properties and failure of thermal barrier coatings with the use of finite element methods: A review. *J Eur Ceram Soc* 2016, **36**: 1313–1331.

[17] Shen W, Wang FC, Fan QB, *et al.* Finite element simulation of tensile bond strength of atmospheric plasma spraying thermal barrier coatings. *Surf Coat Technol* 2011, **205**: 2964–2969.

[18] Bolelli G, Candeli A, Koivuluoto H, *et al.* Microstructure-based thermo-mechanical modelling of thermal spray coatings. *Mater Design* 2015, **73**: 20–34.

[19] Zhao Y, Shinmi A, Zhao X, *et al.* Investigation of interfacial

properties of atmospheric plasma sprayed thermal barrier coatings with four-point bending and computed tomography technique. *Surf Coat Technol* 2012, **206**: 4922–4929.

[20] Wang LL, Fan QB, Liu YB, *et al.* Simulation of damage and failure processes of thermal barrier coatings subjected to a uniaxial tensile load. *Mater Design* 2015, **86**: 89–97.

[21] Ahmadian S, Browning A, Jordan EH. Three-dimensional X-ray micro-computed tomography of cracks in a furnace cycled air plasma sprayed thermal barrier coating. *Scripta Mater* 2015, **97**: 13–16.

[22] Zhu Q, He W, Chen L, *et al.* Interfacial toughness evaluation of thermal barrier coatings by bending test. *Theor Appl Mech Lett* 2018, **8**: 3–6.

[23] Zhu Q, He W, Zhu JG, *et al.* Investigation on interfacial fracture toughness of plasma-sprayed TBCs using a three-point bending method. *Surf Coat Technol* 2018, **353**: 75–83.

[24] Li C, Jacques SDM, Chen Y, *et al.* Precise strain profile measurement as a function of depth in thermal barrier coatings using high energy synchrotron X-rays. *Scripta Mater* 2016, **113**: 122–126.

[25] Fan XL, Zhang WX, Wang TJ, *et al.* The effect of thermally grown oxide on multiple surface cracking in air plasma sprayed thermal barrier coating system. *Surf Coat Technol* 2012, **208**: 7–13.

[26] Zhang WX, Fan XL, Wang TJ. The surface cracking behavior in air plasma sprayed thermal barrier coating system incorporating interface roughness effect. *Appl Surf Sci* 2011, **258**: 811–817.

[27] Zhu W, Zhang ZB, Yang L, *et al.* Spallation of thermal barrier coatings with real thermally grown oxide morphology under thermal stress. *Mater Design* 2018, **146**: 180–193.

[28] Zhu JG, Chen W, Xie HM. Simulation of residual stresses and their effects on thermal barrier coating systems using finite element method. *Sci China Phys Mech Astron* 2015, **58**: 1–10.

[29] Jiang JS, Wang WZ, Zhao XF, *et al.* Numerical analyses of the residual stress and top coat cracking behavior in thermal barrier coatings under cyclic thermal loading. *Eng Fract Mech* 2018, **196**: 191–205.

[30] Zhu JG, Xie HM, Li YJ, *et al.* Interfacial residual stress analysis of thermal spray coatings by miniature ring-core cutting combined with DIC method. *Exp Mech* 2014, **54**: 127–136.

[31] Sharma R, Mahajan P, Mittal RK. Fiber bundle push-out test and image-based finite element simulation for 3D carbon/carbon composites. *Carbon* 2012, **50**: 2717–2725.

[32] Sharma R, Mahajan P, Mittal RK. Elastic modulus of 3D carbon/carbon composite using image-based finite element simulations and experiments. *Compos Struct* 2013, **98**: 69–78.

[33] Drach B, Tsukrov I, Gross T, *et al.* Numerical modeling of carbon/carbon composites with nanotextured matrix and 3D pores of irregular shapes. *Inter J Solids Struct* 2011, **48**: 2447–2457.

[34] Ali J, Farooqi JK, Buckthorpe D, *et al.* Comparative study of predictive FE methods for mechanical properties of nuclear composites. *J Nucl Mater* 2009, **383**: 247–253.

[35] Zhu JG, Yan GS, He GL, *et al.* Fabrication and optimization of micro-scale speckle patterns for digital image correlation. *Meas Sci Technol* 2015, **27**: 015203.

[36] Cernuschi F, Bison PG, Marinetti S, *et al.* Thermophysical, mechanical and microstructural characterization of aged free-standing plasma-sprayed zirconia coatings. *Acta Mater* 2008, **56**: 4477–4488.

[37] Bale HA, Haboub A, MacDowell AA, *et al.* Real-time quantitative imaging of failure events in materials under load at temperatures above 1600 ℃. *Nat Mater* 2012, **12**: 40–46.

[38] Stamopoulos AG, Tserpes KI, Pantelakis SG. Pantelakis. Multiscale finite element prediction of shear and flexural properties of porous CFRP laminates utilizing X-ray CT data. *Theor Appl Fract Mec* 2018, **97**: 303–313.

[39] Agrawal AK, Sarkar PS, Singh B, *et al.* Application of X-ray micro-CT for micro-structural characterization of APCVD deposited SiC coatings on graphite conduit. *Appl Radiat Isotopes* 2016, **108**: 133–142.

[40] Li BH, Tan XQ, Wang FY, *et al.* Fracture and vug characterization and carbonate rock type automatic classification using X-ray CT images. *J Petrol Sci Eng* 2017, **153**: 88–96.

[41] Croom BP, Xu P, Lahoda EJ, *et al.* Quantifying the three-dimensional damage and stress redistribution mechanisms of braided SiC/SiC composites by in situ volumetric digital image correlation. *Scripta Mater* 2017, **130**: 238–241.

[42] Croom B, Wang WM, Li J, *et al.* Unveiling 3D deformations in polymer composites by coupled micro X-ray computed tomography and volumetric digital image correlation. *Exp Mech* 2016, **56**: 999–1016.

[43] Ji ZQ, Haynes JA, Voelkl E, *et al.* Phase formation and stability in reactively sputter deposited yttria-stabilized zirconia coatings. *J Am Ceram Soc* 2001, **84**: 929–936.

[44] Bumgardner C, Croom B, Li XD. High-temperature delamination mechanisms of thermal barrier coatings: In-situ digital image correlation and finite element analyses. *Acta Mater* 2017, **128**: 54–63.

[45] Mao WG, Wang Z, Li CS, *et al.* In-situ characterizations of chemo-mechanical behavior of free-standing vanadium pentoxide cathode for lithium-ion batteries during discharge-charge cycling using digital image correlation. *J Power Sources* 2018, **402**: 272–280.

[46] Heim FM, Zhang YY, Li XD. Uniting strength and toughness of Al matrix composites with coordinated Al_3Ni and Al_3Ti reinforcements. *Adv Eng Mater* 2017, **20**: 1700605.

[47] Heim FM, Croom BP, Bumgardner C, *et al.* Scalable measurements of tow architecture variability in braided ceramic composite tubes. *J Am Ceram Soc* 2018, **101**:

4297–4307.

[48] ABAQUS. ABAQUS/Standard user's manual volumes I-III and ABAQUS CAE manual, version 6.4. Hibbitt, Karlsson & Sorensen, Inc., Pawtucket (USA), 2003.

[49] Liu K, Shi YS, Li CH, *et al.* Indirect selective laser sintering of epoxy resin-Al_2O_3 ceramic powders combined with cold isostatic pressing. *Ceram Int* 2014, **40**: 7099–7106.

[50] Hou YL, Li CH, Wang LL, *et al.* Investigation into the mechanical properties of nanometric zirconia dental ceramics. *Adv Mater Res* 2011, **211–212**: 31–35.

[51] Croom BP, Jin H, Mills B, *et al.* Damage mechanisms in elastomeric foam composites: multiscale X-ray computed tomography and finite element analyses. *Compos Sci Technol* 2019, **169**: 195–202.